scientific reports

Check for updates

OPEN

Numerical simulation based performance enhancement approach for an inorganic BaZrS$_3$/CuO heterojunction solar cell

Ahmed A. El-Naggar[1,2]✉, Lotfy A. Lotfy[1,2], A. A. Felfela[1,2], Walid Ismail[1,2], Mahmoud Abdelfatah[1,2]✉, Swellam W. Sharshir[3] & Abdelhamid El-Shaer[1,2]✉

One of the main components of the worldwide transition to sustainable energy is solar cells, usually referred to as photovoltaics. By converting sunlight into power, they lessen their reliance on fossil fuels and the release of greenhouse gases. Because solar cells are decentralized, distributed energy systems may be developed, which increases the efficiency of the cells. Chalcogenide perovskites have drawn interest due to their potential in solar energy conversion since they provide distinctive optoelectronic characteristics and stability. But high temperatures and lengthy reaction periods make it difficult to synthesise and process them. Therefore, we present the inaugural numerical simulation using SCAPS-1D for emerging inorganic BaZrS$_3$/CuO heterojunction solar cells. This study delves into the behaviour of diverse parameters in photovoltaic devices, encompassing efficiency (η) values, short-circuit current density (J$_{sc}$), fill factor (FF), and open-circuit voltage (V$_{oc}$). Additionally, we thoroughly examine the impact of window and absorber layer thickness, carrier concentration, and bandgap on the fundamental characteristics of solar cells. Our findings showcase the attainment of the highest efficiency (η) values, reaching 27.3% for our modelled devices, accompanied by J$_{sc}$ values of 40.5 mA/cm^2, V$_{oc}$ value of 0.79 V, and FF value of 85.2. The efficiency (η) values are chiefly influenced by the combined effects of V$_{oc}$, J$_{sc}$, and FF values. This optimal efficiency was achieved with CuO thickness, band gap, and carrier concentration set at 5 μm, 1.05 eV, and above 10^{19} cm^{-3}, respectively. In comparison, the optimal parameters for BaZrS$_3$ include a thickness of 1 μm, a carrier concentration below 10^{20} cm^{-3}, and a band gap less than 1.6 eV. Therefore, in the near future, the present simulation will simultaneously provide up an entirely novel field for the less defective perovskite solar cell.

Keywords Inorganic p–n heterojunction, CuO, BaZrS$_3$, Solar cell simulator capacitance software (SCAPS-1D), Thickness, Bandgap, Carrier concentration

Governments across the world are relying more and more on renewable energy as a critical technology to handle energy-related environmental issues, such as lowering CO_2 emissions[1]. Numerous OECD nations, most notably the US and Europe (where state policies and the EU Renewables Directive are prominently shown), have robust plans and objectives in place[2]. Renewable energy is also clearly supported by policy in developing countries such as China, India, and Brazil. The major focus is on the 'new' renewables: solar photovoltaics (PV), wind, and modern biomass[3]. While some of these technologies have made great strides and led to cost savings and rapid market expansion, others still need further research before they can be applied in a commercial setting[4,5].

Solar photovoltaic (PV) energy systems were first utilised in space, but they are now widely used to generate electricity wherever it is needed[6]. Photovoltaic energy production is one of the most efficient and promising forms of renewable energy generation. Because PV technology has a little environmental effect, it is growing in popularity as a power generation method. Right now, hydropower and wind power are the two most widely used renewable energy sources in the world, with solar energy technology coming in third[7–9]. Additionally, the production of electricity using solar photovoltaic (PV) energy sources results in low carbon emissions, which

[1]Physics Department, Faculty of Science, Kafrelsheikh University, Kafrelsheikh 33516, Egypt. [2]Nano Science and Technology Program, Faculty of Science, Kafrelsheikh University, Kafrelsheikh 33516, Egypt. [3]Mechanical Engineering Department, Faculty of Engineering, Kafrelsheikh University, Kafrelsheikh 33516, Egypt. ✉email: ahmed.adel_a691@sci.kfs.edu.eg; mahmoud.abdelfatah@sci.kfs.edu.eg; elshaer@sci.kfs.edu.eg

reduces their impact on global warming[10]. Furthermore, power generated from fossil fuels emits between 400 and 1000 g of CO_2 equivalent per kilowatt-hour (g CO_2 eq/kWh), while silicon-based solar panels result in zero CO_2 emissions[11]. Due to its clean, efficient, environmentally friendly, and reliable nature, solar energy through photovoltaic technology has a great deal of promise for supplying the world's energy needs in the future. PV panels that can produce sustainable energy on a global scale are in high demand due to the considerable increase in popularity of solar PV power in recent decades. Estimates indicate that by the end of the century, PV-generated electricity will surpass other global energy sources[12].

Currently, the most efficient way to use solar radiation to generate energy is to employ multi-junction solar cells made of III–V compound semiconductors. Previous study has achieved efficiencies of up to 39% when exposed to concentrated sunshine[13]. These solar cells were initially designed to power satellites in space, but they are currently being used in conjunction with photovoltaic concentrator systems to investigate the market for terrestrial energy[14]. This generates an enormous potential market for compound semiconductor materials because of the vast regions required to catch adequate solar energy[15]. Concentrator systems based on III–V solar cells have demonstrated environmental friendliness and may be crucial to the future generation of sustainable energy[16].

Modern society may be thought of having been built on semiconductors. Among other things, they are widely used in solar cells, power electronics, computer circuits, optical sensors, solid-state lasers, and light emitting diodes (LEDs). With a total of four levels of cation and anion coordination, covalent materials make up the vast majority of conventional semiconductors. However, because they compete with conventional semiconductors for photovoltaics in a way never seen before, organic–inorganic halide perovskites have garnered a lot of attention in the last 10 years[17–24]. These ionic materials have stronger coordination, which increases the Coulomb attraction between cations and anions. Strong ionicity is hypothesised to mitigate the risk of non-radiative carrier recombination resulting from deep level anti-site defects. Compared to ordinary semiconductors, halide perovskites have extraordinarily long carrier lifetimes (around 1 μs) and extremely low carrier concentrations (10^{13} cm^{-3})[25]. The efficiency of converting power in halide perovskite solar cells has experienced a remarkable growth, rising from 3.8% in 2009 to over 25% in 2019 Chalcogenide perovskite, a unique kind of semiconductor with the general formula ABX_3, was recently found. It is made up of the following parts: A = Ca, Sr, Pb, Ba, Zn, Mg, Cd, Sn, and B = Zr, Hf, Sn, Si, Ge, Pb, Ti, and X = Se, S. They have a lower ionic concentration than oxides or halides, but they nevertheless have a higher ion concentration than regular semiconductors. These perovskite types have not received much attention despite being synthesised more than 50 years ago[26–32], leading to a scarcity of knowledge on their physical attributes[33–35]. Following the screening of theory work, the chalcogenide materials ABX_3 situation changed[36–38]. Numerous compounds with straight band gaps, high absorption rates, and favourable carrier mobility were found in the studies, suggesting that they may find use in optoelectronics. Numerous chalcogenide perovskites, including $CaZrS_3$, $SrZrS_3$, $BaZrS_3$, $SrHfS_3$ and $SrTiS_3$, have been successfully synthesised. According to theoretical expectations, the chalcogenide perovskite $BaZrS_3$, with an orthorhombic structure and a Pnma space group, crystallises with unit-cell parameters of a = 7.04, b = 9.98, and c = 7.05 and exhibits substantial light absorption[39,40]. Crucially, it was discovered that the material showed resistance to pressure, oxidation, and moisture[41].

Several ABX_3 chalcogenide perovskites with appropriate band gaps and absorption characteristics have been discovered for use in photovoltaics. Lately, researchers have been interested to the chalcogenide perovskite compound $BaZrS_3$[42,43]. This compound is recognised as a novel class of photovoltaic semiconductors, whose gap value influences panel efficiency. $BaZrS_3$, the prototype chalcogenide perovskite, with a linear band gap of 1.8 eV and significant near edge absorption[44]. Due to their remarkable chemical stability and absorption of visible light, chalcogenide perovskites (CPs), namely Barium Zirconium Sulphide ($BaZrS_3$), have garnered considerable attention as a competitive alternative to hybrid halide perovskites in optoelectronics[45]. $BaZrS_3$, a stable, non-toxic chalcogenide perovskite, is gaining attention for thin-film photovoltaic (PV) applications due to its superior stability and does not contain toxic elements compared to lead halide perovskites[46].

One interesting oxide semiconductor is cupric oxide, often known as copper monoxide (CuO). Among other semiconducting oxides, It is a promising selective solar absorber due to its high solar absorbency and low thermal emittance[47,48]. It is suitable to solar cell applications due to its 1.2 eV optical band gap and its easy conversion to a p type material. In addition, it has a straight band gap, a high absorption coefficient, is readily synthesised, is inexpensive, abundant, and environmentally benign. Actually, the first CuO semiconductor humidity sensor was created in 1931 by Braver et al[5,49]. Due to its potential applications in lithium-ion batteries, flexible supercapacitors, optoelectronics, catalysis, fuel sensors, and as a superior absorbent to remove very harmful ions from ground water, this material has lately attracted a lot of attention.

The current study is working through the solar cell simulator capacitance program (SCAPS-1D) to study a highly efficient n–i–p CPs model solar cell[44,50]. SCAPS software is designed for the simulation of one-dimensional solar cells, specifically heterojunction and thin-film photovoltaic solar cells, enabling accurate modeling and simulation[51].

Consequently, we are presenting SCAPS numerical simulations for novel inorganic $BaZrS_3$/CuO heterojunction solar cell systems for the first time. In particular, we will investigate in detail how the window and absorber layers' bandgap, carrier concentration and thickness affect the fundamental characteristics of the solar cell. The results of our simulation will be a major first step towards determining the perfect conditions for high-efficiency solar device production.

Structure of the apparatus and simulation approach

In this study, CPs-based n–p planar perovskite device models have been constructed using solar cell simulator capacitance software structure (SCAPS-1D, version 3.3.07). In the manufacture of our inorganic p–n heterojunction solar cells, we often use an n-$BaZrS_3$ thin film as the window layer and a p-CuO thin film as the absorber

layer in order to solve the poisson and continuity equations. The device's front and back metal contacts were made of transparent conductive oxide (FTO) and gold (Au). A schematic diagram of the heterojunction device structure used in the simulation is shown in Fig. 1.

Parameters used in the simulation

This research's main objective is to use the Solar Cell Capacitance Simulator Structures (SCAPS-1D) programme to simulate and analyse our inorganic solar cells. This programme is an advanced and useful numerical modelling tool designed to help comprehend and make sense of how solar systems actually function[46,52–54]. SCAPS software is a common choice for studying perovskite solar cells (PSCs) since it has advantages over alternatives such as Silvaco Atlas and GVPDM.SCAPS is free and open-source, offering a user-friendly interface and comprehensive manual, compared to the steep learning curve of Silvaco Atlas and GVPDM. SCAPS is flexible and customizable, allowing users to modify input parameters, material properties, and device structures according to their needs. It is fast and accurate, providing reliable results in a short time, unlike Silvaco Atlas and GVPDM, which are slow and complex, requiring more computational resources and time[55–57]. The construction and manufacturing of a solar cell device involve careful consideration of various parameters. These factors encompass the band gap, thickness, electron affinity, State effective densities in the valence band (V_B) and conduction band (C_B), dielectric permittivity, electron and hole mobilities, as well as shallow acceptor and donor densities (referred to as doping concentration and denoted as N_A and N_D, respectively), and defect density N_t. Exploring different values for these input variables is essential to identify optimal conditions for achieving enhanced performance in solar cell devices. Additionally, it is assumed that parameters like electron and hole thermal velocities remain consistent across all layers, each equal to 10^7 cm/s. A detailed list of these parameters is provided in Table 1[46,58,59], as well as the contact parameters used in the simulation are listed in Table 2[60,61].

However, the AM 1.5 light spectrum's intensity of light (100 mW/cm^2) was utilised in all SCAPS-1D simulation calculations under standard testing conditions (STC). Using the following ratio, the continuity and poisson equations for electrons and holes were applied in SCAPS-1D[62,63].

$$\frac{d^2}{dx^2}\Psi(x) = \frac{e}{\varepsilon_0\varepsilon_r}\left(p(x) - n(x) + N_D - N_A + \rho_p - \rho_n\right) \tag{1}$$

$$\frac{dJ_n}{dx} = G - R \quad \text{and} \quad \frac{dJ_p}{dx} = G - R \tag{2}$$

In this situation, the variables e (electron charge), Ψ (electrostatic potential), ε_0 (vacuum permittivity), ε_r (relative permittivity), p (hole density), n (electron density), ρ_n (electron distribution), ρ_p (hole distribution), J_n (electron current densities), J_p (hole current densities), R (recombination rate), and G (generation rate) are denoted.
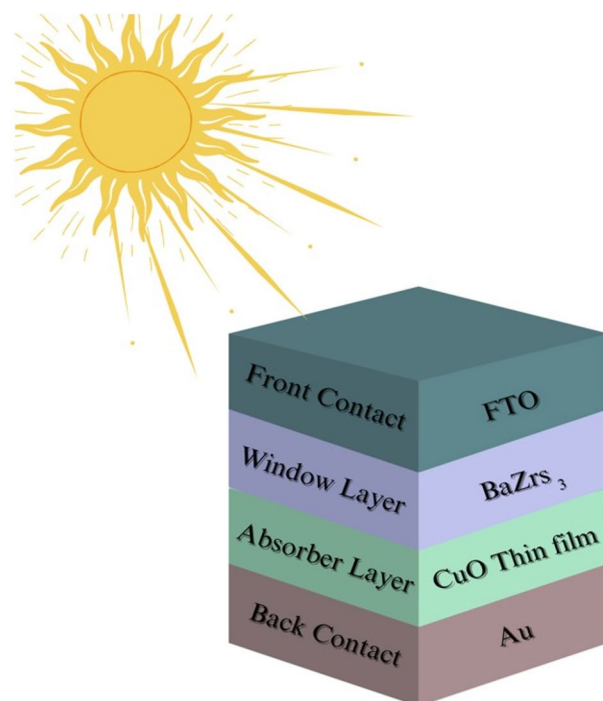

Figure 1. The structure of inorganic BsZrS$_3$/CuO heterojunction solar cell.

Parameter of the material	n-BaZrS$_3$	p-CuO
Thickness (nm)	500	100
Dielectric permittivity	9.6	18.1
Bandgap (eV)	1.76	1.2
Electron affinity (eV)	4.10	4.07
Effective density of states of valence band maximum (cm^{-3})	1.8×10^{19}	5.5×10^{20}
Effective density of states of conduction band minimum (cm^{-3})	2.2×10^{18}	3×10^{19}
Acceptor concentration (cm^{-3})	0	10^{16}
Donor concentration (cm^{-3})	Wide range	0
Mobility of hole (cm^2/(V s))	5.58	20
Mobility of electron (cm^2/(V s))	11.3	200
Electron thermal velocity (cm/s)	10^7	10^7
Hole thermal velocity (cm/s)	10^7	4.6×10^6
Deffect density N$_t$ (cm^{-3})	Wide range	1×10^5

Table 1. Primary input parameters employed in the SCAPS-1D simulation for each material[46,58,59].

Contacts	Back metal contact properties (Au)	Front metal contact Properties (FTO)
Metal work function (eV)	4.98	4.07
Surface recombination velocity of electron (cm/s)	1.000×10^7	1.000×10^7
Surface recombination velocity of hole (cm/s)	1.000×10^7	1.000×10^7

Table 2. The simulation's contact parameters[60,61].

Findings and analysis

Analysis of the effects of CuO thickness, bandgap, and carrier concentration on the fundamental solar cell characteristics

Changing the absorber layer band gap, thickness, and carrier concentrations will have an initial influence on important photovoltaic variables that we are going to explore in this section. Specifically, we analyse the variations in open-circuit voltage (V$_{oc}$), short-circuit current density (J$_{sc}$), fill factor (FF), and cell efficiency (η). Throughout these investigations, we keep the window layer band gap, thickness, and carrier concentrations constant at values of 1.7 eV, 0.2 μm and 10^{19} cm^{-3}, respectively.

As indicated in Fig. 2a, the open-circuit voltage (V$_{oc}$) rises from roughly 0.6 V at a bandgap (E$_g$) of 1 eV to approximately one V at an Eg of 1.5 eV. Meanwhile, the changes in V$_{oc}$ with CuO thickness, spanning from 1 to 6 μm for any E$_g$, do not exceed 0.1 V.

As depicted in Fig. 2b, the short-circuit current density (J$_{sc}$) exhibits a decline, decreasing from approximately 25.7–4.3 mA/cm^2 as the bandgap (E$_g$) increases from 1 to 1.5 eV. Notably, the J$_{sc}$ values remain relatively consistent across various CuO thicknesses, ranging from 0.5 to 6 μm.

In Fig. 2c, the fill factor (FF) values exhibit diverse trends. Firstly, there is a decrease from approximately 85.9% to about 81.4% as the bandgap (E$_g$) increases from 1 to 1.5 eV, while increasing the thickness of CuO (thinner CuO thin films) from approximately 0.1–1.5 μm. Secondly, there is an increase from about 85.9% to approximately 87.3% with an increase in E$_g$ from 1 to 1.5 eV. This is accompanied by a marginal 0.5% decrease in FF value as CuO thickness increases from roughly 1.5–6 μm (thicker CuO thin films).

In Fig. 2d, distinct zones with varying values are observed. A performance of approximately 12.2% is identified at a bandgap (E$_g$) of about 1 eV, covering thicknesses ranging from about 0.5 to 6 μm. Across nearly every variation of E$_g$ from 1 to 1.5 eV, an average value of approximately 11.2% is achieved, With the exception of the region with thickness between 2 and 6 μm and E$_g$ between 1.3 and 1.45 eV, where a better performance of about 13.1% is obtained.

As per the provided equation, a rise in the band gap enhances the local collection efficiency of light absorption at the interface between the n-BaZrS$_3$ thin film and the p-CuO thin film. This improvement leads to an augmented carrier generation rate, ultimately resulting in a notable increase in the V$_{oc}$ value[64].

$$V_{oc} = \frac{k_B T}{q} \ln \left(1 + \frac{I_{ph}}{I_0} \right) \tag{3}$$

Furthermore, considering the bandgap values of BaZrS$_3$ and CuO, an anticipated enhancement in the charge separation process is expected owing to a cliff-like band alignment[65]. The conduction band offset (ΔE$_c$) value decreases as the bandgap energy increases because the valence band (E$_v$) shifts downward and the conduction band (E$_c$) shifts upward[65]. By making it easier for promoted electrons to travel from the absorber layer to the window layer interface, this decrease in ΔE$_c$ promotes charge separation and raises V$_{oc}$[65]. Additionally, an increase in band gap results in significant hole concentrations near the interface junction. As a result, the likelihood of
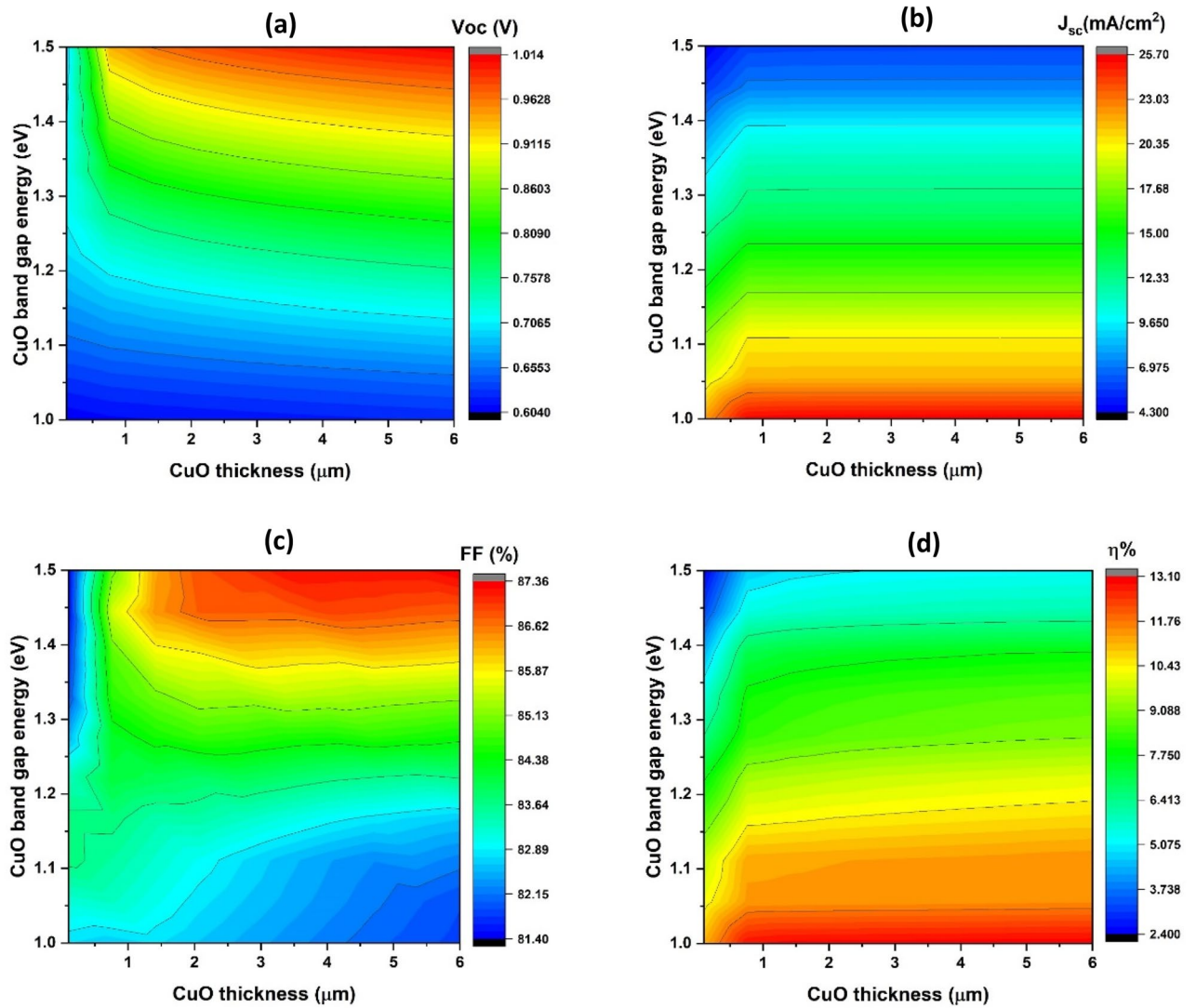
Figure 2. The basic characteristics of simulated solar cells with the absorber layer thickness (x-axis) and carrier concentration (y-axis).

recombination is increased due to heightened surface and interface recombination. This, in turn, accounts for the observed decrease in short-circuit current density (J_{sc})[65,66]. Moreover, the formation of charge carrier capture centers takes place due to the wavefunction crossover between vibrationally excited states of lower and higher-lying electronic states[66].

Fill factor (FF) behavior is always affected by a number of parameters, but the series and shunt resistances are particularly important. The V_{oc} values also play a role, albeit to a lesser extent, as illustrated in the following equation[67].

$$FF = \frac{\upsilon_{oc} - \ln(\upsilon_{oc} + 0.72)}{\upsilon_{oc} + 1} \tag{4}$$

where $\upsilon_{oc} = qV_{oc}/AkT$

The behavior of η and values of V_{oc}, J_{sc}, and FF can be illustrated using the equation provided below[68].

$$\eta = \frac{FFV_{oc}J_{sc}}{P_{in}} \tag{5}$$

Based on the preceding data, we have inferred that, for enhanced solar cell efficiency, it is advisable to maintain the CuO band gap between 3 and 6 μm in thickness and 1.05 eV in range. As a result, as shown in Fig. 3, we generated JV curves that represent the essential properties of solar cells as a function of CuO thickness, which ranges from 3 to 6 μm, while maintaining a constant band gap of 1.05 eV. It clearly indicates that V_{oc} ranges from 0.616 to 0.623 V, J_{sc} remains constant at 25.6 mA/cm², FF varies between 81.7 and 82.3%, and η ranges
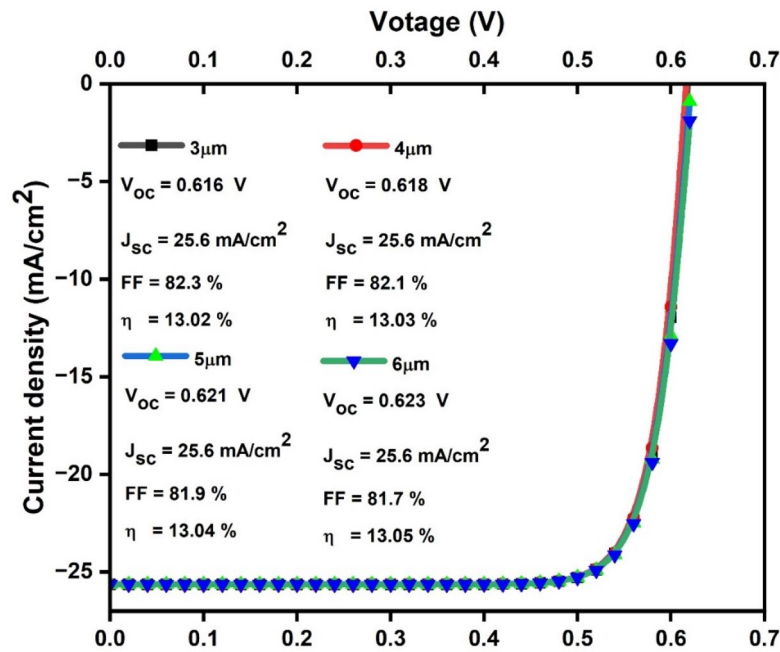
Figure 3. Modelled JV curves with basic characteristics of solar cells as a function of CuO thickness in the range of 3–6 μm.

from 13.02 to 13.05 each having a thickness that increases from 3 to 6 μm. Notably, the η values closely follow the trends observed in V_{oc} and FF values.

Figure 4 shows a contour plot with the obtained photovoltaic parameters V_{oc}, J_{sc}, FF, and η as functions of the carrier concentration from 10^{14}–10^{21} cm^{-3} (y-axis) and CuO thin film thickness from 1 to 6 μm (x-axis).

As depicted in Fig. 4a, the open-circuit voltage (V_{oc}) rises from approximately 0.6–0.84 V as the acceptor concentration increases from 10^{14} to 10^{21} cm^{-3}. There are only minimal variations in V_{oc} values as CuO thickness increases.

According to Fig. 4b, the short-circuit current density (J_{sc}) increases from approximately 23.3–25.8 mA/cm^2 when the acceptor concentration remains constant, ranging from 10^{17} to 10^{21} cm^{-3}. It maintains constancy at around 25.5 mA/cm^2 for carrier concentrations below 10^{20} and for CuO thicknesses exceeding 0.6 μm. For CuO thicknesses less than 0.6 μm, the J_{sc} remains approximately 22.3 mA/cm^2 for carrier concentrations exceeding 10^{20} cm^{-3}, but the J_{sc} value varies with CuO thickness, ranging from 23.3 to 25.8 mA/cm^2 for carrier concentrations below 10^{20} cm^{-3}.

In Fig. 4c, it is observed that the fill factor (FF) demonstrates an increase with thickness, reaching approximately 84.1–86.5% within the thickness range of 1–6 μm. For a thickness greater than 1 μm and a carrier concentration of 10^{21} cm^{-3}, the FF is notably higher at around 86.5%, indicating a positive correlation with thickness. This suggests that FF values mostly remain constant, hovering around 84.15%, for a carrier concentration of 10^{20} cm^{-3}, and decrease with increasing thickness for carrier concentrations below 10^{20} cm^{-3}.

Figure 4d illustrates that the values of η exhibit an increase from approximately 15.2% to about 18.7% with an increase in carrier concentration from 10^{19} to 10^{21} cm^3 and as the thickness increases. The η value remains constant at 13.2% when the concentration of the carriers is less than 10^{19} cm^{-3}. A thickness greater than 3 μm and a carrier concentration of 10^{21} cm^{-3} result in the higher η value of roughly 18.7%.

With the increase in carrier concentration, From the p-CuO thin film to the n-BaZrS$_3$ thin film, there is increased electron diffusion. Consequently, the device's built-in voltage (V_{bi}), primarily determined by the depletion width (W_d), experiences amplification, leading to a significant rise in V_{oc}. Additionally, the increase in photogenerated current (electron–hole pairs) (I_{ph}) contributes to the reverse saturation current increasing and the recombination rate decreasing(I_o)[69]. This phenomenon is reflected in Eq. (3), which elucidates the correlation between V_{oc}, I_{ph}, and I_o, demonstrating how an increase in carrier concentration results in higher V_{oc} values. On the contrary, as the carrier concentration increases, there is an increase in the population of photogenerated charge carriers and a simultaneous reduction in both leakage current and recombination current[70]. This effect is particularly noticeable for CuO thicknesses exceeding 1.6 μm.

When the carrier concentration exceeds 10^{19} cm^{-3} and the absorber thickness is less than 1.6 μm, there is an increase in J_{sc} with CuO thickness. This rise in thickness can be attributed to the charge-collecting length of CuO, enhancing the junction's electron–hole pair collecting[71]. It indicates that as the thickness increases, the charge carriers are more effectively separated and stored. When the carrier concentration is above 10^{19} cm^{-3} and the CuO thickness surpasses 1.6 μm, the charge-collecting length is maximized. This leads to an increased probability of carrier collection, a reduction in recombination rate, and a decrease in leakage current, resulting in larger J_{sc} values[65]. As demonstrated in Eq. (5), the behavior of η can be understood as the combined effect of V_{oc}, J_{sc}, and FF, with η being a function of these parameters[68].
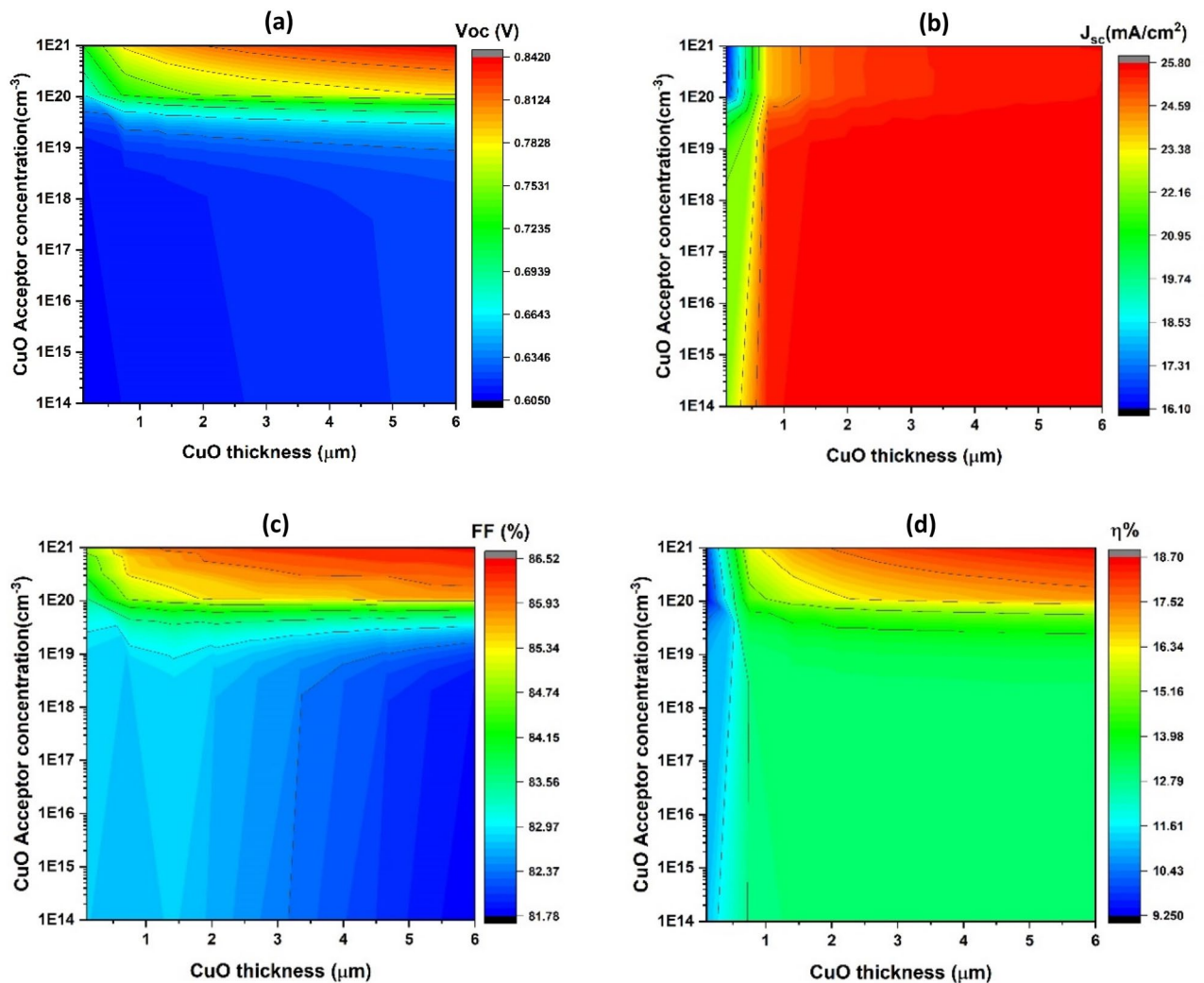
Figure 4. Fundamental parameters of simulated solar cells, including V_{oc} (**a**), J_{sc} (**b**), FF (**c**), and η (**d**), with a constant bandgap (E_g) of 1.05 eV, as functions of the (absorber layer thickness on the x-axis) and (carrier concentration on the y-axis).

In this scenario, the shape of EQE predominantly mirrors the shape of J_{sc}, as acceptor concentration primarily influences photogenerated current. Consequently, It is determined what the external quantum efficiency (EQE) is in relation to the band gap, carrier concentration, and CuO thickness, as depicted in Fig. 5. With EQE at 0% at 200 nm and 100% at 800 nm, it is clear that all CuO thicknesses follow a comparable pattern. The greater EQE component's area under the curve drops from 1200 to 800 nm when the band gap raises from 1 to 1.5 eV, and it increases by raising the carrier concentration from 10^{14} to 10^{21} cm^{-3}. In addition, there is an intrinsic absorption edge in the short-wavelength region of the spectrum. Variations in carrier concentration along with reflection off the Au back contact may cause these edges to shift in position.

Studies show that when high-energy photons are present, the photogenerated current rises and decreases with low-energy photons, suggesting varying rates of creation and recombination of charge carriers that impact J_{sc}. These findings validate and suggest that η is primarily influenced by J_{sc}. Based on the preceding calculations, it can be inferred that for BaZrS$_3$/CuO heterojunction solar cell devices to achieve higher efficiencies, the optimal ranges for CuO, thickness, carrier concentration and band gap are approximately 5 μm, above 10^{19} cm^{-3} and 1.05 eV, respectively.

Impact of bandgap, carrier concentration, and thickness of BaZrS$_3$ on fundamental solar cell characteristics

Furthermore, we will explore the impact of variations in the thickness, bandgap, and carrier concentrations of the BaZrS$_3$ thin film, serving as the window layer, on crucial features of photovoltaic devices. Meanwhile, the thickness of the CuO layer, bandgap, and carrier concentrations will be held constant at 5 μm, 1.05 eV, and 10^{19} cm^{-3}, respectively.
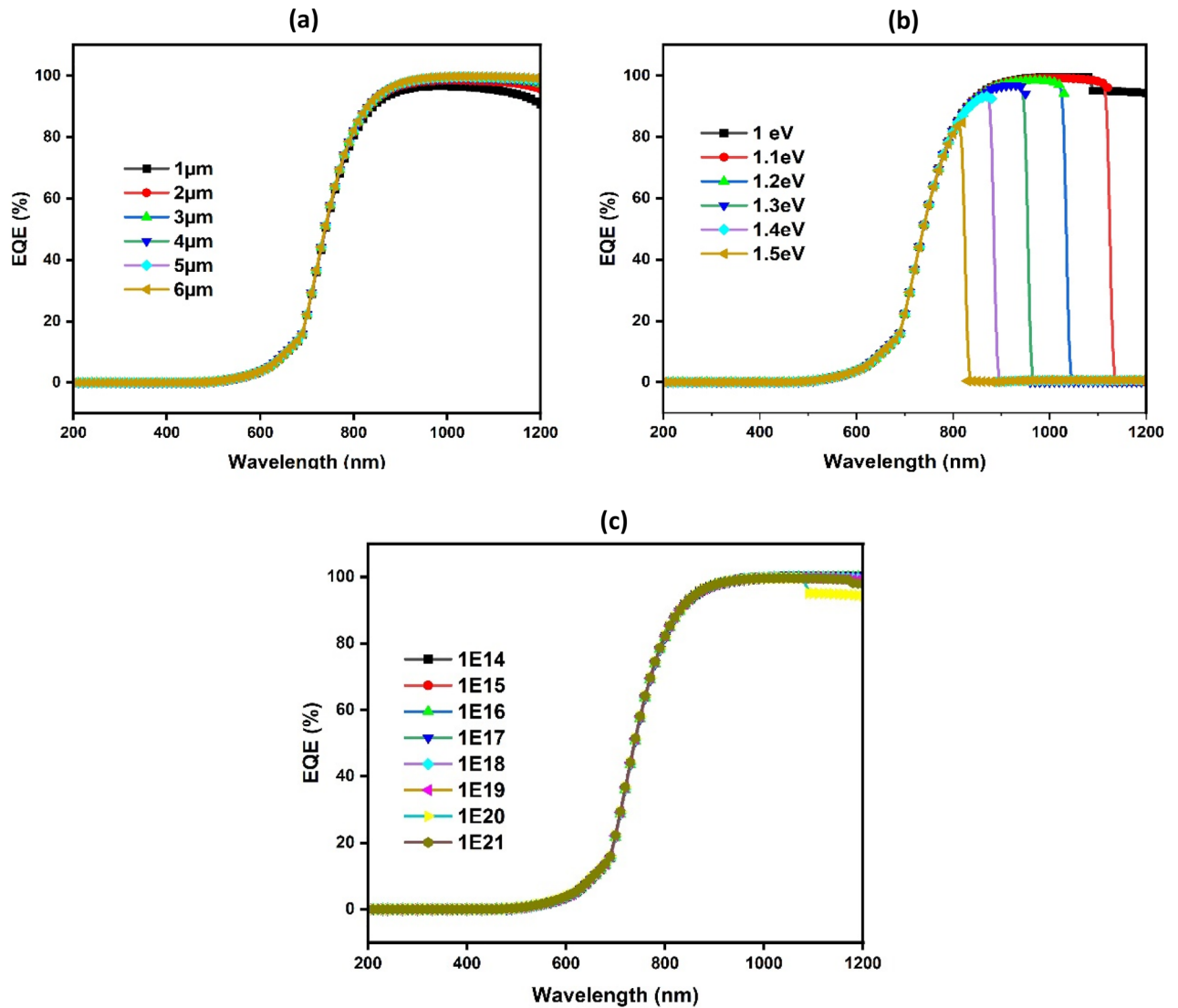
Figure 5. Simulated external quantum efficiency with CuO thickness (**a**), band gap (**b**), and carrier concentration (**c**), respectively.

Figure 6 presents a contour map reflecting the simulated fundamental characteristics of a solar cell, illustrating how these properties change as the bandgap (which varies from 1.3 to 1.8 eV on the y-axis) and $BaZrS_3$ thin film thickness (which ranges from 0.1 to 1 μm on the x-axis) change.

Figure 6a illustrates the variations in open-circuit voltage (V_{oc}) at different points. Specifically, as thickness increases from 0.1 to 1 μm, it drops from roughly 0.79 V to roughly 0.77 V, with the maximum V_{oc} observed at approximately 0.1 μm thickness. Furthermore, for smaller band gaps ranging from 1.3 eV to around 1.6 eV, there is an improvement in the V_{oc} value at each bandgap value.

The J_{sc} values in Fig. 6b follow a similar pattern to the V_{oc}, decreasing from around 41.2 mA/cm^2 to approximately 22.8 mA/cm^2 as thickness increases from 0.1 to 1 μm. The peak J_{sc} is observed at approximately 0.1 μm in thickness. Lower band gaps ranging from 1.3 eV to about 1.6 eV lead to an increase in the J_{sc} value for each corresponding bandgap value.

In Fig. 6c, the FF values exhibit multiple zones where the FF increases from 84.96 to 85.82% as the thickness increases from 0.1 to 1 μm. An average FF value of approximately 85.8% is achieved for nearly all variations of the E_g from 1.3 to 1.8 eV, except for the zone situated at the E_g from 1.4 to 1.5 eV and the thickness from 0.6 to 1 μm, which attains a higher performance of around 85.8%.

In Fig. 6d, the η values exhibit a similar trend to the V_{oc}, where η decreases from around 27.85% to about 15.2% as the thickness increases from 0.1 to 1 μm. For band gaps less than 1.6 eV and thicknesses less than 0.1 μm, an average value of approximately 27% is observed.

The obtained results can be understood in the following manner: More light enters the interface junction when the band gap increases, leading to a higher rate of photogenerated charge carriers. This, in turn, facilitates the separation and collection of carriers, while concurrently reducing both recombination current and leakage current. These combined effects contribute to an elevation in the V_{oc} value, particularly for band gaps less
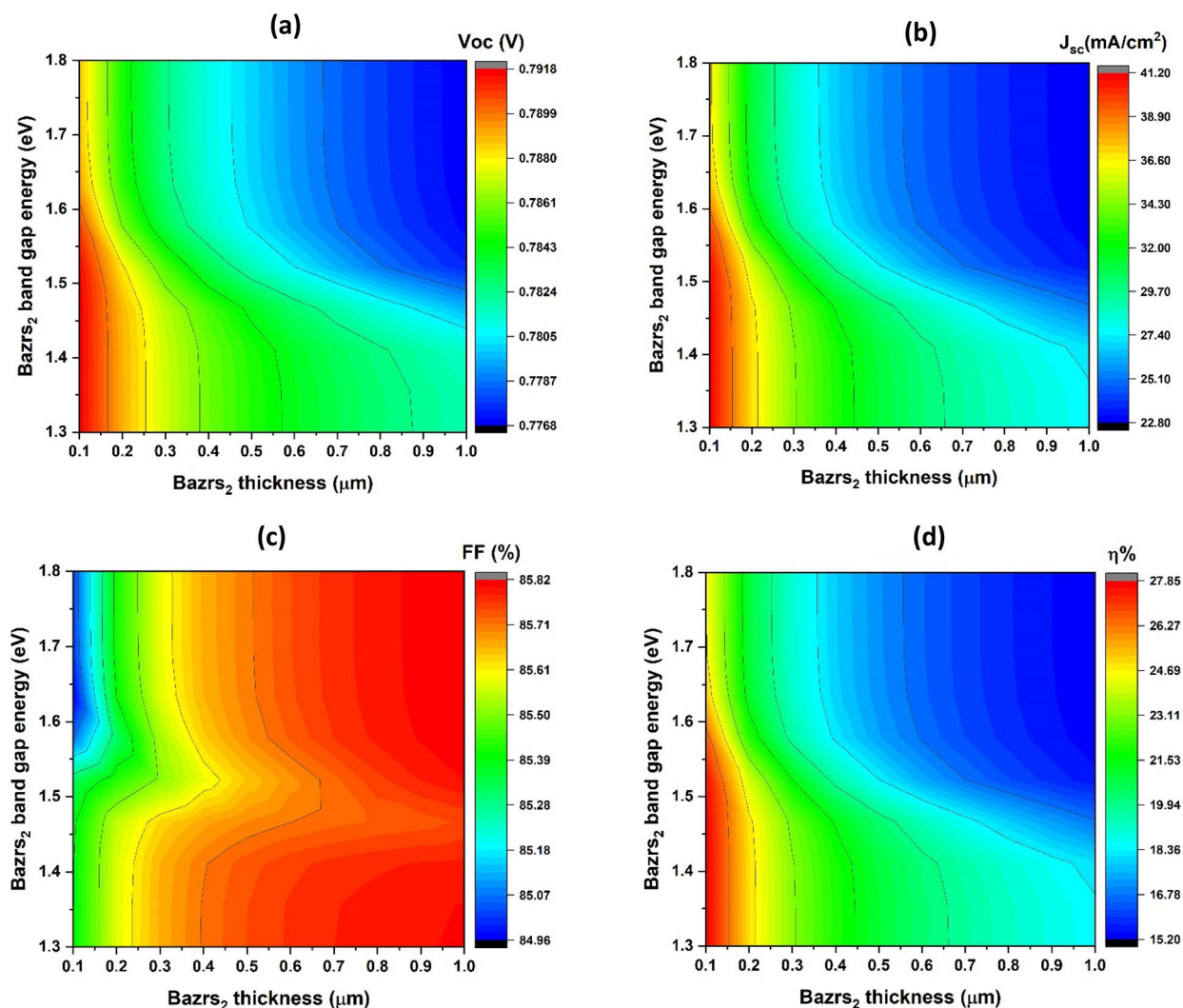
Figure 6. Critical parameters of simulated solar cells, showcasing open-circuit voltage (V_{oc}) (**a**), short-circuit current density (J_{sc}) (**b**), fill factor (FF) (**c**), and efficiency (η) (**d**) with respect to the band gap (y-axis) and window layer thickness (x-axis), maintaining a constant donor concentration of 10^{19} cm^{-3}.

than 1.6 eV, as explained in Eq. (3)[64]. Moreover, the reduction in the V_{oc} value is associated with an increase in thickness. This augmentation promotes the generation of electron–hole pairs across the junction by extending the charge collection length[71]. Additionally, bandgap alignment plays a crucial role in enhancing the V_{oc} value. Smaller band gaps in BaZrS$_3$, especially those less than 1.6 eV, lead to increased confinement, resulting increasing the current due to increased carrier intra-band tunnelling at the interface voltage barrier[72]. A similar rationale can be applied to explain the behaviour of J_{sc} values.

Increasing the band gap of BaZrS$_3$ leads to a reduction in both V_{oc} and J_{sc} values. This is attributed to an increase in the recombination process and leakage current, particularly noticeable as the thickness of BaZrS$_3$ increases[65,66]. The mismatch between the band gaps of CuO and BaZrS$_3$ in this scenario results in the creation of capture centres, promoting carrier recombination[66].

As indicated in Eq. (4), the behaviour of the fill factor (FF) can be explained by its inverse relationship with V_{oc} values. The efficiency (η) values are predominantly influenced by the combined effects of V_{oc}, J_{sc}, and FF values, as outlined in Eq. (4)[68].

Our findings suggest that maintaining the thickness of BaZrS$_3$ between 0.1 and 0.2 μm, decreasing with thickness, and setting the band gap below 1.6 eV can enhance device efficiency.

Under these conditions, as shown in Fig. 7, the thickness increases from 0.1 to 0.4 μm, the fill factor (FF) ranges from 85.2 to 85.6%, the efficiency (η) decreases from 27.3 to 18.7%, the open-circuit voltage (V_{oc}) varies between 0.78 and 0.79 V, and the short-circuit current (J_{sc}) decreases from 40.5 to 27.9 mA/cm^2.

Figure 8 depicts a contour plot demonstrating variations in critical solar cell characteristics, where the carrier concentration ranges from 10^{14} to 10^{21} cm^{-3} on the y-axis and the BaZrS$_3$ thin film thickness, which ranges from 0.1 to 1 μm, is the dependent variable.
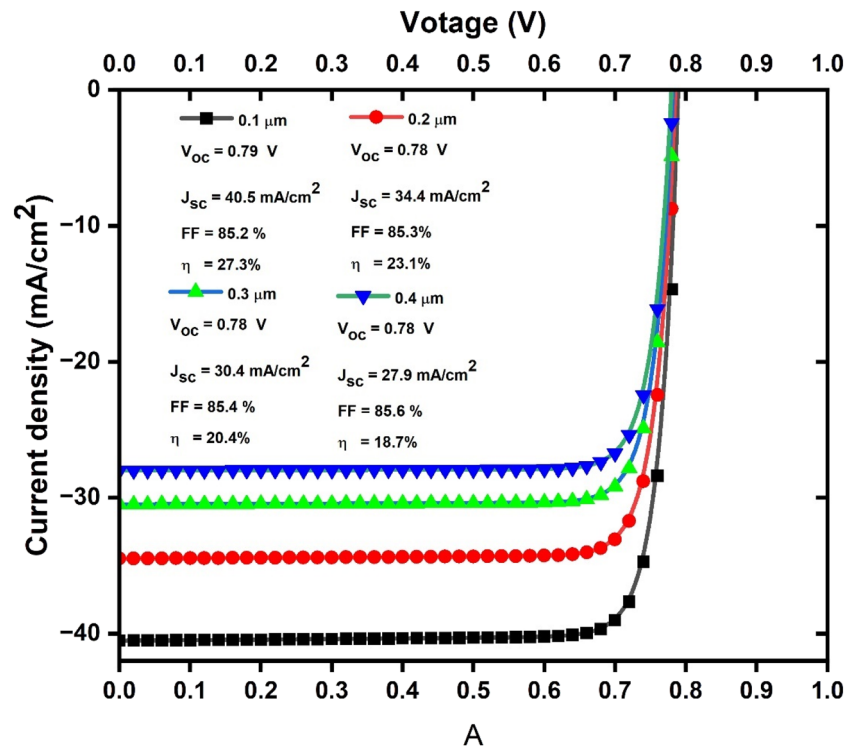
Figure 7. Current–voltage (JV) curves of solar cell devices with BaZrS$_3$ thickness varied from 0.1 to 0.4 μm.

The study of Fig. 8a demonstrates that the open-circuit voltage (V$_{oc}$) varies across distinct regions. More precisely, it falls from roughly 0.79 V to roughly 0.77 V as thickness rises from 0.1 to 1 μm, while the highest V$_{oc}$ reached at thickness approximately 0.1 μm. When carrier concentrations are less than 10^{20} cm^{-3}, the V$_{oc}$ value improves for each given carrier concentrations value.

Figure 8b indicates that the J$_{sc}$ values follow the same pattern as the V$_{oc}$, with J$_{sc}$ decreasing from approximately 42.5 mA/cm^2 to approximately 22.8 mA/cm^2 as thickness increases from 0.1 to 1 μm and the highest J$_{sc}$ attained at thickness of approximately 0.1 μm. The J$_{sc}$ value improves for each individual carrier concentration value when the carrier concentration is less than 10^{19} cm^{-3}. According to Fig. 8c the FF value remained constant at around 85.8% for carrier concentrations more than 10^{20} cm^{-3} with increasing BaZrS$_3$ thickness. The FF value rises from 0.1 to 1 μm as the thickness increases when the carrier concentration is less than 10^{20} cm^{-3}. In contrast, the FF reached its maximum value for levels of carrier concentration greater than 10^{20} cm^{-3}. Figure 8d, demonstrate that the η values have the same form as the V$_{oc}$, which decreases from about 27.2% to about 15.2% as the thickness increases from 0.1 to 1 μm, while the highest achieved at thickness around 0.1 μm. The value improves for every individual carrier concentration value in the event that the carrier concentration is below 10^{19} cm^{-3}.

The data clearly show that increasing the donor concentrations of the BaZrS$_3$ thin film decreases the V$_{oc}$ value as the thickness increases, especially when the concentration is less than 10^{19} cm^{-3} for each thickness. This absence of influence could be due to the entire establishment of the depletion width (W$_d$), which influences the charge carrier generation rate and minority carrier diffusion length. The flow of electrons in the p-CuO layer and holes in the n-BaZrS$_3$ layer influences the photogenerated current significantly[65]. The full built-in voltage (V$_{bi}$) and the depletion width (W$_d$), primarily determined on the p-CuO thin film side, are directly associated with this current[64]. For each given carrier concentration below 10^{20} cm^{-3}, the V$_{oc}$ value drops as the BaZrS$_3$ thickness increases. This is due to the longer lifetime and larger charge collection channel, which results in enhanced photogenerated current while concurrently decreasing leakage current and recombination rates as thin film thickness increases[71].

These observations are corroborated by the fact that raising the carrier concentration above 10^{20} cm^{-3} results in a drop in J$_{sc}$ value, even while the thickness increases. Furthermore, the decrease in J$_{sc}$ is due to the window layer predominantly functioning as a conducting channel for electrons rather than contributing considerably to solar spectrum absorption[73].

The efficiency (η) values provide a complete view of performance through the combination of V$_{oc}$, J$_{sc}$, and FF, with its value predominantly following V$_{oc}$ and FF trends. As shown in Fig. 9, photogenerated current is investigated by simulating EQE as a function of BaZrS$_3$ band gap, carrier concentration and thickness.

It is clear that EQE drops from approximately 18% to nearly zero as thickness increases from 0.1 to 0.6 m, particularly at higher energy levels, and from approximately 18% to almost zero when energy levels increase from 1.3 to 1.8 eV, particularly at longer wavelengths. This decrease in EQE with band gap and thickness is caused by an increase in recombination rate, which lowers charge carrier collection and, in turn, lowers the produced current's separation[74]. It is important to note that, independent of carrier concentration, EQE has the same shape
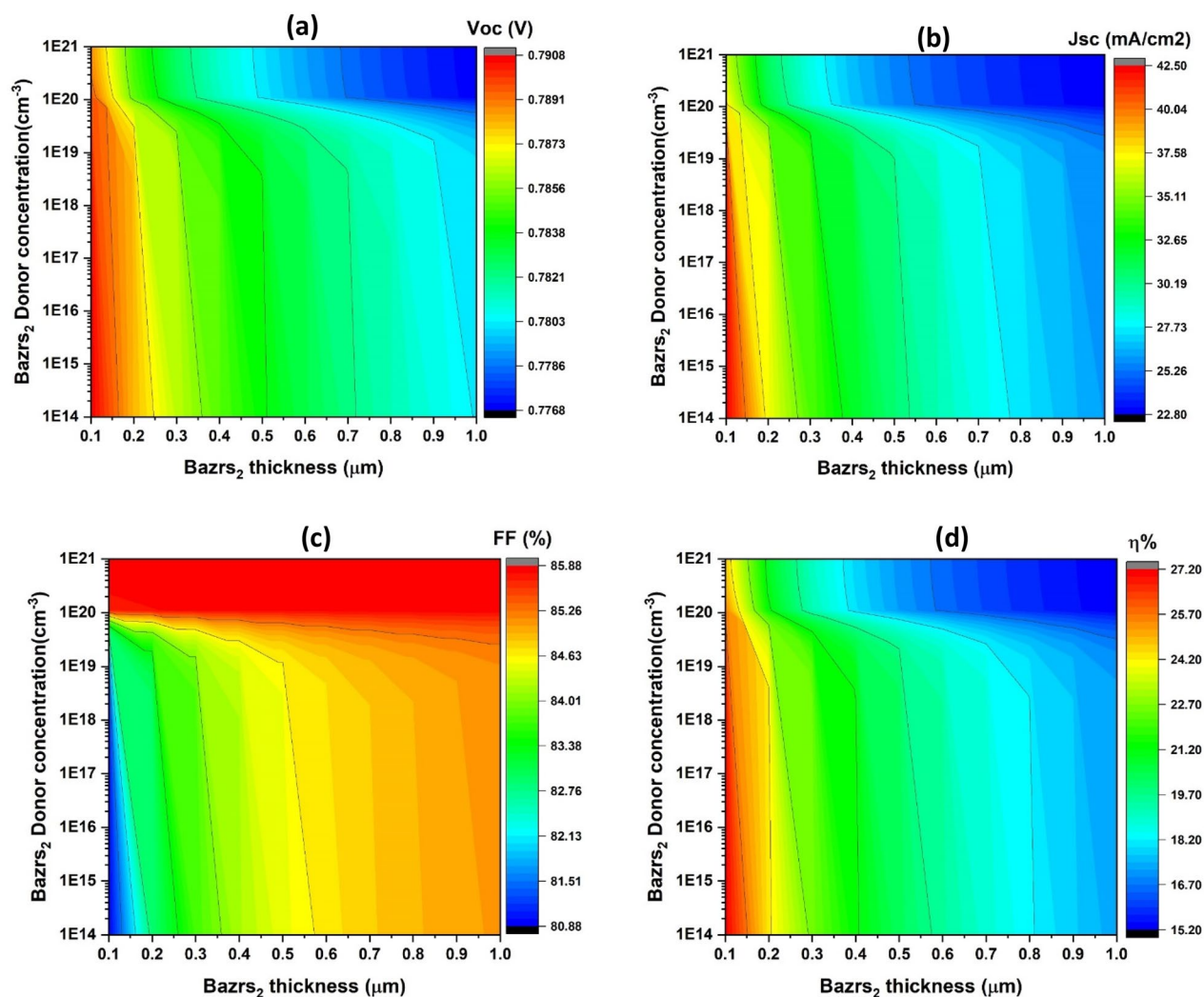
Figure 8. Critical parameters of simulated solar cells; open-circuit voltage (V_{oc}) (**a**), short-circuit current density (J_{sc}) (**b**), fill factor (FF) (**c**), and efficiency (η) (**d**) with respect to the band gap (y-axis) and window layer thickness (x-axis), maintaining a constant donor concentration of 10^{19} cm^{-3}.

and value. The values of J_{sc} for the obtained BaZrS$_3$ thin film band gap, carrier concentrations and thickness are consistent with and supported by the EQE results.

Additionally, our modelling outcomes indicate that the ideal values for CuO band gap, carrier concentration and thickness in inorganic BaZrS$_3$/CuO heterojunction solar cell devices should be approximately 1.05 eV, above 10^{19} cm^{-3} and 5 μm, respectively. In comparison, the optimal parameters for BaZrS$_3$ are a thickness of 1 μm, a carrier concentration of less than 10^{20} cm^{-3}, and a band gap of less than 1.6 eV. With a V_{oc} value of 0.79 V, a J_{sc} value of 41.2 mA/cm^2 and an FF value of 85.8%, the maximum efficiency was attained under these conditions.

Our results show that solar cell devices based on BaZrS$_3$/CuO could compete with those based on In$_2$S$_3$. By contrast, Cu(In, Ga)Se$_2$, CuIn(S,Se)$_2$, and Cu$_2$ZnSnS$_4$-based solar cells with In$_2$S$_3$ as the buffer layer (thickness: 50–125 nm), fluorine-doped tin oxide as the window layer, and gold (Au) as the back contact showed the best efficiency, ranging from 16.94 to 22.50%[75]. Reyes et al. also created an n–i–p heterojunction perovskite solar cell with the following configuration: FTO/TiO$_2$/MASnI$_3$/Cu$_2$ZnSnS$_4$/Au. The best values were obtained with donner and acceptor densities of 10^{16} cm^{-3} and 10^{14} cm^{-3}, respectively, and comprised a J_{sc} of 31.66 mA/cm^2, a V_{oc} of 0.96 V, an FF of 67%, and an efficiency (η) of 20.28%[76].

Effect of operating temperature on JV curves and the fundamental specifications of the ideal BaZrS$_3$/CuO solar cell

In this section, we examined the impact of operational temperature on the JV curves and key parameters of the most efficient BaZrS$_3$/CuO solar cell, as illustrated in Fig. 10. It is evident that an increase in operational temperature leads to a reduction in both V_{oc} and J_{sc}, resulting in a decrease in the overall efficiency (η). These values decrease from 0.834 to 0.747 V, 43.67 to 43.41 mA/cm^2, and 30.2% to 26.2% as the temperature rises from 260 to 340 K, respectively.
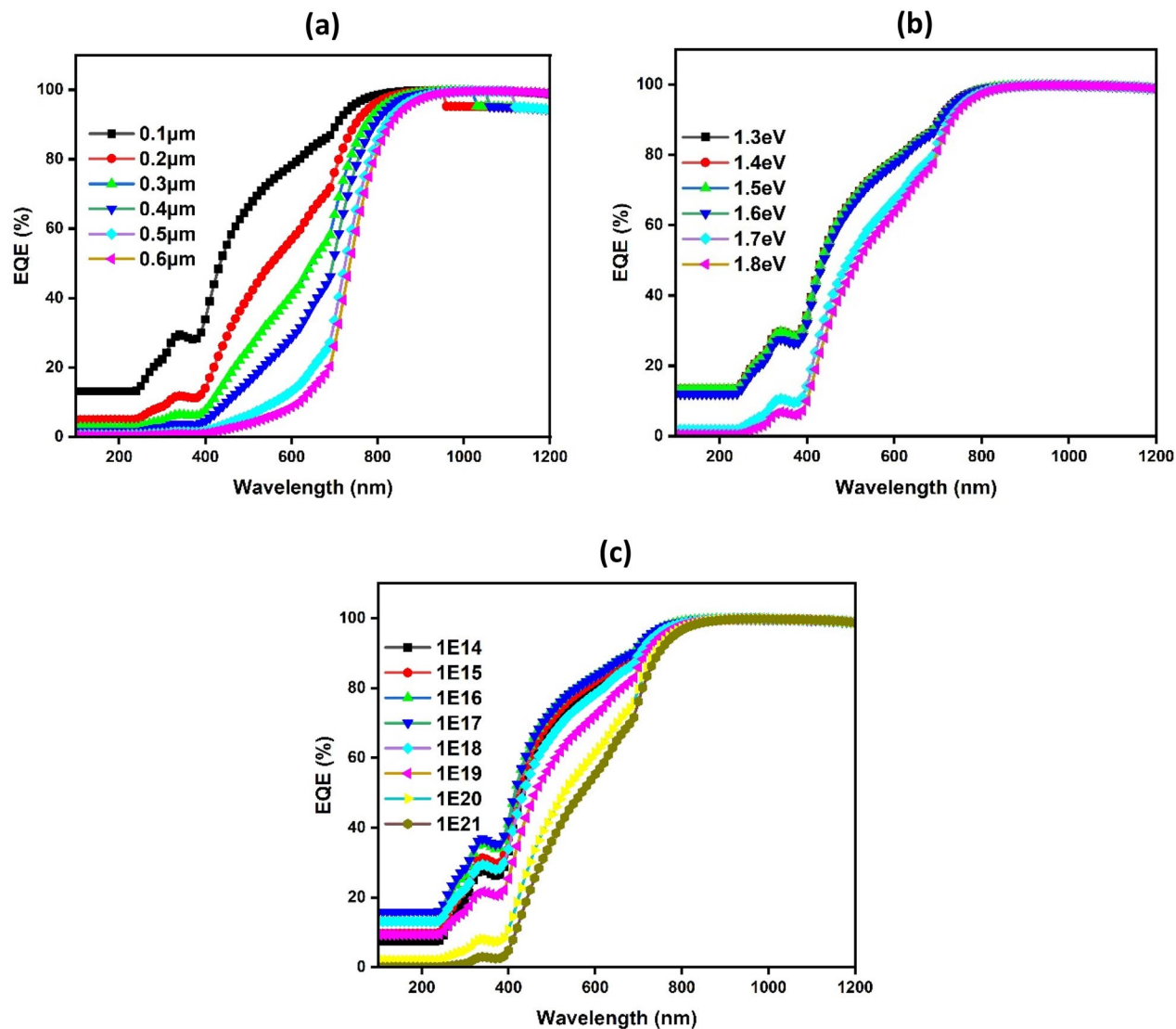
Figure 9. Simulated (EQE) as dependent variables of BaZrS$_3$ thickness (**a**), Band gap (E$_g$) (**b**), and carrier concentration (**c**).

The results shown can be clarified through Eq. (3), in which the reverse saturation current (I$_o$) increases with increasing temperature, as does the chance of charge carrier recombination. As a result, V$_{oc}$, J$_{sc}$, and value all fall. It is worth mentioning, however, that the variation in η is relatively small, especially when compared to average global temperatures. Under typical temperature settings, the BaZrS$_3$/CuO solar cell may still be a feasible option for making high-performance photovoltaic systems.

Table 3 highlights the simulated photovoltaic performance of various device structures, showcasing distinct voltage, current density, fill factor, and efficiency metrics. Notably, the work stands out with a device structure featuring FTO/BaZrS$_3$/CuO/Au, exhibiting promising characteristics with a voltage at open circuit of 0.79 V, a short-circuit current density of 40.5 mA/cm^2, a fill factor of 85.2%, and an efficiency of 27.03%.

Comparing these results to prior studies, it's evident that different device architectures yield varying performance outcomes. For instance, while some configurations demonstrate higher V$_{OC}$ or J$_{SC}$ values, this structure exhibits a competitive combination of these parameters, alongside a notable FF and the efficiency. This suggests the potential of BaZrS$_3$/CuO as an active layer in photovoltaic devices, particularly in achieving balanced performance across key metrics.

Conclusions

Chalcogenide perovskites have emerged as promising materials with unique optoelectronic characteristics and enhanced stability, garnering increasing interest among researchers. However, challenges such as high-temperature requirements and lengthy reaction durations have constrained the synthesis and processing of these materials.

To address this, we present the initial numerical simulation using SCAPS-1D for novel inorganic BaZrS$_3$/CuO heterojunction solar cells. Copper oxide has low thermal emittance and strong solar absorbency, making
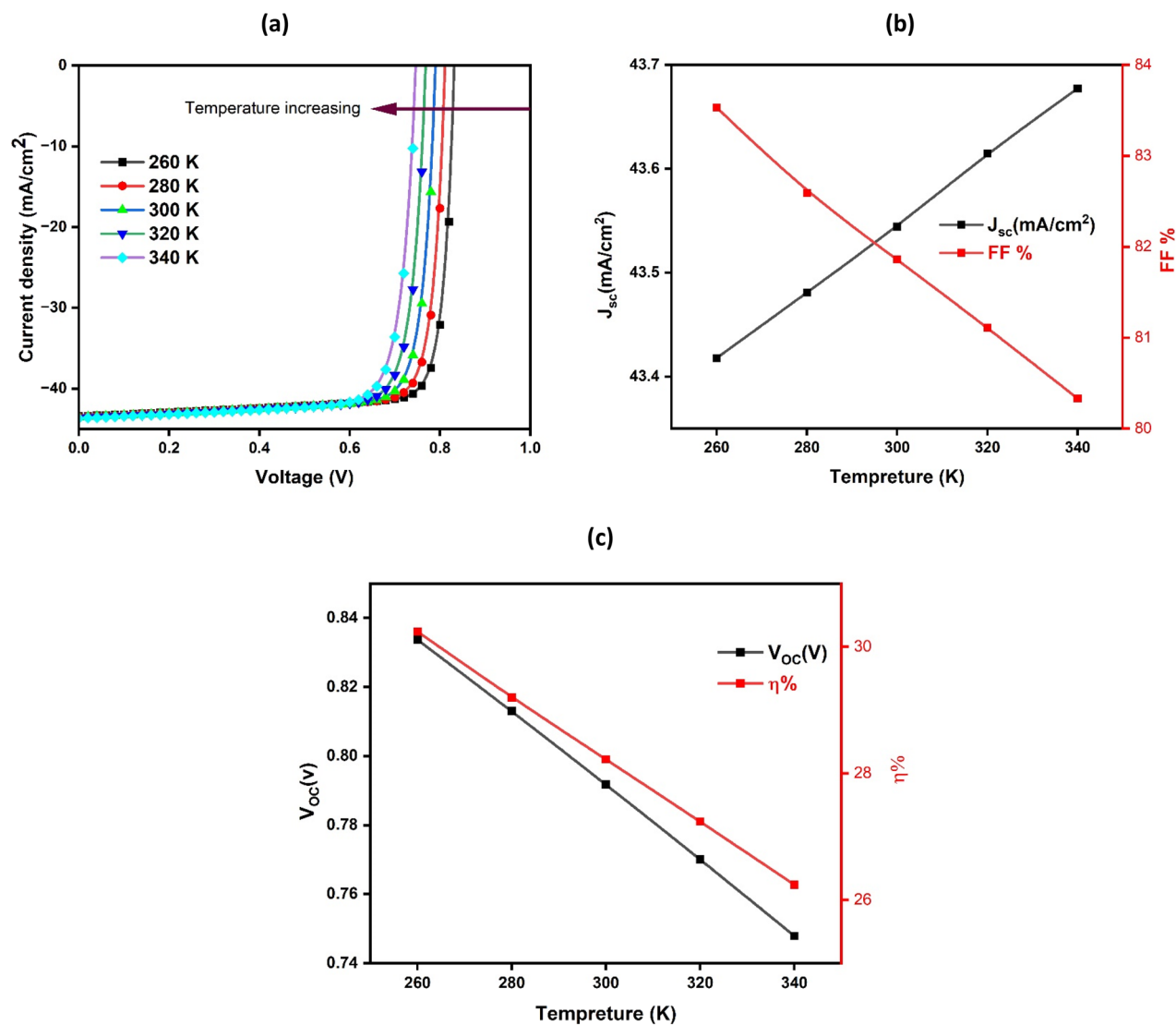
(a)   **(b)**

(c)

Figure 10. Simulated JV curves and crucial variables of the optimal $BaZrS_3$/CuO solar cell, showcasing their variations with operational temperature, measured in Kelvin (K).

Device structure	Voltage at Open Circuit V_{OC} (V)	Short-circuit current density J_{SC} (mA/cm²)	Fill factor FF (%)	Efficiency η (%)	References
FTO/MAPbl$_3$/Au	0.823	17.53	82.67	12.35	[35]
ITO/ZnO/MAGeI$_3$/Spiro- OMeTAD/Au	1.74	16.27	64.51	18.3	[54]
FTO/TiO$_2$/BaZrS$_3$/Cu$_2$O/Au	1.16	12.24	87.13	12.42	[46]
FTO/TiO$_2$/BaZrS$_3$/Spiro-OMeTAD/Au	1.21	16.54	86.26	17.29	[77]
FTO/TiO$_2$/BaZrS$_3$/CuSbS$_2$/W	1.00	22.57	73.7	17.13	[78]
TCO/Zrs$_2$/CuO/Au	0.96	34.2	72.2	23.08	[58]
FTO/TiO$_2$/Ba(Zr$_{0.87}$,Ti$_{0.12}$)S$_3$/Cu$_2$O/back contact	1.09	26.57	85.78	24.86	[79]
FTO/TiO$_2$/BaZrSe$_3$/Spiro-OMeTAD/Au	0.72	46.65	77.32	25.84	[80]
AZO/i-ZnO/CdS/Ba(Zr$_{0.95}$,Ti0$_{.05}$)S$_3$/a-Si	1.26	27.06	88.47	30.06	[81]
FTO/ZrS$_2$/BaZrS$_3$/SnS/Pt	1.18	29.74	80.15	28.17	[82]
FTO/ BaZrS$_3$/CuO/Au	0.79	40.5	85.2	27.03	This work

Table 3. Comparison of the current simulation result with the predicted maximum PSG for photovoltaic performance.

it a viable selective solar absorber among the various semiconducting oxides being studied. And, compared to lead halide perovskites, $BaZrS_3$, a stable, non-toxic chalcogenide perovskite, is becoming increasingly common for thin-film photovoltaic applications because of its superior stability and absence of hazardous components.

This study comprehensively explores various parameters in photovoltaic devices, encompassing efficiency (η), short-circuit current density (J_{sc}), fill factor (FF), and open-circuit voltage (V_{oc}). We also thoroughly investigate the impact of window and absorber layer thickness, carrier concentration, and bandgap on the fundamental characteristics of solar cells. Our outcomes reveal that factors such as built-in voltage (V_{bi}), depletion width (W_d), charge carrier collecting length, photogenerated current, minority carrier lifetime, and recombination rate significantly influence solar cell performance.

Our results demonstrate the attainment of the highest efficiency (η) values, reaching 27.3% for our modeled devices, accompanied by J_{sc} values of 40.5 mA/cm^2, V_{oc} value of 0.79 V, and FF value of 85.2. The Fill factor (FF) is influenced by series and shunt resistances and exhibits an inverse relationship with V_{oc} values. The efficiency (η) values are predominantly influenced by the combined effects of V_{oc}, J_{sc}, and FF values. This optimal efficiency was achieved with CuO thickness, band gap, and carrier concentration set at 5 μm, 1.05 eV, and above 10^{19} cm^{-3}, respectively.

In comparison, the optimal parameters for $BaZrS_3$ include a thickness of 1 μm, a carrier concentration below 10^{20} cm^{-3}, and a band gap less than 1.6 eV. Our simulated results underscore the growing attention toward organic–inorganic halide perovskites in photovoltaics due to their potential for high efficiency, large-scale, low-cost fabrication, and reduced non-radiative carrier recombination. These perovskites exhibit stronger coordination, enhancing Coulomb attraction between cations and anions, contributing to their favourable properties.

Future work
We can Investigate the effect of different metal contacts, such as Ag, Cu, Fe and C on the performance and stability of $BaZrS_3$/CuO PSCs and exploring the potential of other chalcogenide perovskites, such as $BaSnS_3$, $BaTiS_3$, and $BaHfS_3$, as absorber materials for PSCs.

Data availability
The datasets used and/or analyzed during the current study available from the corresponding author on reasonable request.

References
1. Gielen, D. *et al.* The role of renewable energy in the global energy transformation. *Energy Strategy Rev.* **24**, 38–50. https://doi.org/10.1016/j.esr.2019.01.006 (2019).
2. Nicolli, F. & Vona, F. Energy market liberalization and renewable energy policies in OECD countries. *Energy Policy* **128**, 853–867. https://doi.org/10.1016/j.enpol.2019.01.018 (2019).
3. Li, L. *et al.* Review and outlook on the international renewable energy development. *Energy Built Environ.* **3**, 139–157. https://doi.org/10.1016/j.enbenv.2020.12.002 (2022).
4. Gross, R., Leach, M. & Bauen, A. Progress in renewable energy. *Environ. Int.* **29**, 105–122. https://doi.org/10.1016/S0160-4120(02)00130-7 (2003).
5. Nerle, U. & Rabinal, M. K. Thermal oxidation of copper for favorable formation of cupric oxide (CuO) semiconductor. *IOSR J. Appl. Phys.* **5**, 1–7 (2013).
6. Lupangu, C. & Bansal, R. C. A review of technical issues on the development of solar photovoltaic systems. *Renew. Sustain. Energy Rev.* **73**, 950–965. https://doi.org/10.1016/j.rser.2017.02.003 (2017).
7. Paiano, A. Photovoltaic waste assessment in Italy. *Renew. Sustain. Energy Rev.* **41**, 99–112. https://doi.org/10.1016/j.rser.2014.07.208 (2015).
8. Sinke, W. C. *et al.* A strategic Research Agenda for Photovoltaic Solar Energy Technology (2007).
9. Jäger-Waldau, A. J. *PV Status Report 2019*, 7–94 (2019).
10. Agency, I. E. *Energy Technology Perspectives 2014* (2014).
11. Shin, J., Park, J. & Park, N. A method to recycle silicon wafer from end-of-life photovoltaic module and solar panels by using recycled silicon wafers. *Sol. Energy Mater. Sol. Cells* **162**, 1–6. https://doi.org/10.1016/j.solmat.2016.12.038 (2017).
12. Xu, Y., Li, J., Tan, Q., Peters, A. L. & Yang, C. Global status of recycling waste solar panels: A review. *Waste Manag.* **75**, 450–458. https://doi.org/10.1016/j.wasman.2018.01.036 (2018).
13. Philipps, S. P., Dimroth, F. & Bett, A. W. In *McEvoy's Handbook of Photovoltaics* 3rd edn (ed. Kalogirou, S. A.) 439–472 (Academic Press, 2018).
14. Philipps, S. P. & Bett, A. W. III–V multi-junction solar cells. In *Advanced Concepts in Photovoltaics* Vol. 11 (eds Nozik, A. J. *et al.*) 87–117 (Royal Society of Chemistry, 2014).
15. Philipps, S. P. & Bett, A. W. III–V multi-junction solar cells and concentrating photovoltaic (CPV) systems. In *Advanced Optical Technologies* Vol. 3 (ed. Pfeffer, M.) 469–478 (De Gruyter, 2014).
16. Dimroth, F. High-efficiency solar cells from III–V compound semiconductors. *Phys. Status Solidi C* **3**, 373–379. https://doi.org/10.1002/pssc.200564172 (2006).
17. Liu, M., Johnston, M. B. & Snaith, H. J. Efficient planar heterojunction perovskite solar cells by vapour deposition. *Nature* **501**, 395–398. https://doi.org/10.1038/nature12509 (2013).
18. Zhou, H. *et al.* Interface engineering of highly efficient perovskite solar cells. *Science* **345**, 542–546. https://doi.org/10.1126/science.1254050 (2014).
19. Dong, Q. *et al.* Electron-hole diffusion lengths > 175 μm in solution-grown $CH_3NH_3PbI_3$ single crystals. *Science* **347**, 967–970. https://doi.org/10.1126/science.aaa5760 (2015).
20. Grätzel, M. The light and shade of perovskite solar cells. *Nat. Mater.* **13**, 838–842. https://doi.org/10.1038/nmat4065 (2014).
21. Jeon, H.-S. *et al.* Improving the efficacy of chlorhexidine-releasing elastomerics using a layer-by-layer coating technique. *Dent. Mater. J.* **36**, 476–481. https://doi.org/10.4012/dmj.2016-337 (2017).
22. Stranks, S. D. *et al.* Electron-hole diffusion lengths exceeding 1 micrometer in an organometal trihalide perovskite absorber. *Science* **342**, 341–344. https://doi.org/10.1126/science.1243982 (2013).

23. Xing, G. *et al.* Long-range balanced electron- and hole-transport lengths in organic-inorganic $CH_3NH_3PbI_3$. *Science* **342**, 344–347. https://doi.org/10.1126/science.1243167 (2013).

24. Bhattarai, S., Pandey, R., Madan, J., Ahmed, F. & Shabnam, S. Performance improvement approach of all inorganic perovskite solar cell with numerical simulation. *Mater. Today Commun.* **33**, 104364. https://doi.org/10.1016/j.mtcomm.2022.104364 (2022).

25. de Quilettes, D. W. *et al.* Impact of microstructure on local carrier lifetime in perovskite solar cells. *Science* **348**, 683–686. https://doi.org/10.1126/science.aaa5333 (2015).

26. Hahn, H. & Mutschke, U. Untersuchungen über ternäre Chalkogenide. XI. Versuche zur Darstellung von Thioperowskiten. *Z. Anorg. Allg. Chem.* **288**, 269–278. https://doi.org/10.1002/zaac.19572880505 (1957).

27. Clearfield, A. J. The synthesis and crystal structures of some alkaline earth titanium and zirconium sulphides. *Acta Crystallogr.* **16**, 135–142 (1963).

28. Lelieveld, R., Ijdo, D. J. & Chemistry, C. Sulphides with the $GdFeO_3$ structure. *Acta Crystallogr. Sect. B Struct. Crystallogr. Cryst. Chem.* **36**, 2223–2226 (1980).

29. Wang, Y., Sato, N. & Fujino, T. Synthesis of $BaZrS_3$ by short time reaction at lower temperatures. *J. Alloys Compd.* **327**, 104–112. https://doi.org/10.1016/S0925-8388(01)01553-5 (2001).

30. Lee, C.-S., Kleinke, K. M. & Kleinke, H. Synthesis, structure, and electronic and physical properties of the two $SrZrS_3$ modifications. *Solid State Sci.* **7**, 1049–1054. https://doi.org/10.1016/j.solidstatesciences.2005.02.010 (2005).

31. Cai, B. *et al.* A class of Pb-free double perovskite halide semiconductors with intrinsic ferromagnetism, large spin splitting and high Curie temperature. *Mater. Horizons* **5**, 961–968. https://doi.org/10.1039/c8mh00590g (2018).

32. Bhattarai, S. *et al.* Comparative study of distinct halide composites for highly efficient cesium-based perovskite solar cells. *Energy Fuels* **37**, 16035–16049. https://doi.org/10.1021/acs.energyfuels.3c02610 (2023).

33. Ishii, M. & Saeki, M. Raman and infrared spectra of $BaTiS_3$ and $BaNbS_3$. *Phys. Status Solidi (b)* **170**, K49–K54. https://doi.org/10.1002/pssb.2221700149 (1992).

34. Ishii, M., Saeki, M. & Sekita, M. Vibrational spectra of barium–zirconium sulfides. *Mater. Res. Bull.* **28**, 493–500. https://doi.org/10.1016/0025-5408(93)90132-W (1993).

35. Bhattarai, S., Sharma, A., Muchahary, D., Gogoi, M. & Das, T. D. Carrier transport layer free perovskite solar cell for enhancing the efficiency: A simulation study. *Optik* **243**, 167492. https://doi.org/10.1016/j.ijleo.2021.167492 (2021).

36. Chen, Y. *et al.* Carbon kagome lattice and orbital-frustration-induced metal-insulator transition for optoelectronics. *Phys. Rev. Lett.* **113**, 085501. https://doi.org/10.1103/PhysRevLett.113.085501 (2014).

37. Niu, S. *et al.* Bandgap control via structural and chemical tuning of transition metal perovskite chalcogenides. *Adv. Mater.* **29**, 1604733. https://doi.org/10.1002/adma.201604733 (2017).

38. Sharma, S. *et al.* Machine learning-aided band gap engineering of $BaZrS_3$ chalcogenide perovskite. *ACS Appl. Mater. Interfaces* **15**, 18962–18972. https://doi.org/10.1021/acsami.3c00618 (2023).

39. Gross, N. *Phonon and Stability Properties in Two Novel Chalcogenide Solids Investigated by Raman Scattering Using High-Pressure and Photocrystallization Experiments* (State University of New York at Buffalo, 2018).

40. Pal, D. *et al.* Numerical investigation of a high-efficiency $BaZr_xTi_{1-x}S_3$ chalcogenide perovskite solar cell. *New J. Chem.* **48**, 2474–2483. https://doi.org/10.1039/D3NJ04832B (2024).

41. Zitouni, H., Tahiri, N., El Bounagui, O. & Ez-Zahraouy, H. Electronic, optical and transport properties of perovskite $BaZrS_3$ compound doped with Se for photovoltaic applications. *Chem. Phys.* **538**, 110923. https://doi.org/10.1016/j.chemphys.2020.110923 (2020).

42. Vincent Mercy, E. N., Srinivasan, D. & Marasamy, L. Emerging $BaZrS_3$ and $Ba(Zr, Ti)S_3$ chalcogenide perovskite solar cells: A numerical approach toward device engineering and unlocking efficiency. *ACS Omega* **9**, 4359–4376. https://doi.org/10.1021/acsomega.3c06627 (2024).

43. Chawki, N. *et al.* Efficacy analysis of $BaZrS_3$-based perovskite solar cells: investigated through a numerical simulation. *Adv. Mater. Process. Technol.* https://doi.org/10.1080/2374068X.2024.2307093 (2024).

44. Yu, Z. *et al.* Chalcogenide perovskite $BaZrS_3$ thin-film electronic and optoelectronic devices by low temperature processing. *Nano Energy* **85**, 105959. https://doi.org/10.1016/j.nanoen.2021.105959 (2021).

45. Osei-Agyemang, E. & Rajan, K. J. Understanding the thermodynamic stability of the [100] surface systems of the photovoltaic chalcogenide perovskite $BaZrS_3$. *J. Phys. Chem. C* **127**, 17146–17156 (2023).

46. Karthick, S., Velumani, S. & Bouclé, J. J. Chalcogenide $BaZrS_3$ perovskite solar cells: A numerical simulation and analysis using SCAPS-1D. *Opt. Mater.* **126**, 112250 (2022).

47. Balık, M., Bulut, V. & Erdogan, I. Y. Optical, structural and phase transition properties of Cu_2O, CuO and Cu_2O/CuO: Their photoelectrochemical sensor applications. *Int. J. Hydrog. Energy* **44**, 18744–18755 (2019).

48. Maruyama, T. Copper oxide thin films prepared by chemical vapor deposition from copper dipivaloylmethanate. *Sol. Energy Mater. Sol. Cells* **56**, 85–92. https://doi.org/10.1016/S0927-0248(98)00128-7 (1998).

49. Aliko, V. *et al.* "From shadows to shores"-quantitative analysis of CuO nanoparticle-induced apoptosis and DNA damage in fish erythrocytes: A multimodal approach combining experimental, image-based quantification, docking and molecular dynamics. *Sci. Total Environ.* **906**, 167698. https://doi.org/10.1016/j.scitotenv.2023.167698 (2024).

50. Pandey, R. *et al.* Halide composition engineered a non-toxic perovskite-silicon tandem solar cell with 30.7% conversion efficiency. *ACS Appl. Electron. Mater.* **5**, 5303–5315. https://doi.org/10.1021/acsaelm.2c01574 (2023).

51. Burgelman, M., Decock, K., Niemegeers, A., Verschraegen, J. & Degrave, S. J., Belgium. *SCAPS Manual* (2016).

52. Burgelman, M., Nollet, P. & Degrave, S. Modelling polycrystalline semiconductor solar cells. *Thin Solid Films* **361–362**, 527–532. https://doi.org/10.1016/S0040-6090(99)00825-1 (2000).

53. Abdelaziz, S., Zekry, A., Shaker, A. & Abouelatta, M. Investigating the performance of formamidinium tin-based perovskite solar cell by SCAPS device simulation. *Opt. Mater.* **101**, 109738. https://doi.org/10.1016/j.optmat.2020.109738 (2020).

54. Bhattarai, S. & Das, T. D. Optimization of carrier transport materials for the performance enhancement of the $MAGeI_3$ based perovskite solar cell. *Sol. Energy* **217**, 200–207. https://doi.org/10.1016/j.solener.2021.02.002 (2021).

55. Rono, N., Merad, A. E., Kibet, J. K., Martincigh, B. S. & Nyamori, V. O. Simulation of the photovoltaic performance of a perovskite solar cell based on methylammonium lead iodide. *Opt. Quantum Electron.* **54**, 317. https://doi.org/10.1007/s11082-022-03737-1 (2022).

56. Baro, M. & Borgohain, P. SCAPS-1D device simulation of highly efficient perovskite solar cells using diverse charge transport layers. *J. Electron. Mater.* **52**, 7623–7644. https://doi.org/10.1007/s11664-023-10681-7 (2023).

57. Sharma, H., Verma, V. K., Singh, R. C., Singh, P. K. & Basak, A. Numerical analysis of high-efficiency $CH_3NH_3PbI_3$ perovskite solar cell with PEDOT:PSS hole transport material using SCAPS 1D simulator. *J. Electron. Mater.* **52**, 4338–4350. https://doi.org/10.1007/s11664-023-10257-5 (2023).

58. Abdelfatah, M. *et al.* SCAPS simulation of novel inorganic ZrS_2/CuO heterojunction solar cells. *Sci. Rep.* **13**, 4553. https://doi.org/10.1038/s41598-023-31553-4 (2023).

59. El-Shafai, N. *et al.* Enhancement of electrochemical properties and photocurrent of copper oxide by heterojunction process as a novel hybrid nanocomposite for photocatalytic anti-fouling and solar cell applications. *Sep. Purif. Technol.* **267**, 118631. https://doi.org/10.1016/j.seppur.2021.118631 (2021).

60. Chen, Q., Ni, Y., Dou, X. & Yoshinori, Y. The effect of energy level of transport layer on the performance of ambient air prepared perovskite solar cell: A SCAPS-1D simulation study. *Crystals* **12**, 68. https://doi.org/10.3390/cryst12010068 (2022).

61. Danladi, E., Kashif, M., Daniel, T., Achem, C. & Gyan, M. J. 7.379% Power conversion efficiency of a numerically simulated solid-state dye-sensitized solar cell with copper(I) thiocyanate as a hole conductor. *East Eur. J. Phys.* **3**, 19–31 (2022).
62. Burgelman, M., Verschraegen, J., Degrave, S. & Nollet, P. Modeling thin-film PV devices. *Prog. Photovolt. Res. Appl.* **12**, 143–153. https://doi.org/10.1002/pip.524 (2004).
63. Mohammed, M., Mazari, H., Khelifi, S., Bouraiou, A. & Dabou, R. Simulation of high efficiency CIGS solar cells with SCAPS-1D software. *Energy Procedia* **74**, 736–744. https://doi.org/10.1016/j.egypro.2015.07.809 (2015).
64. Abdelfatah, M. *et al.* Fabrication and characterization of low cost Cu_2O/ZnO: Al solar cells for sustainable photovoltaics with earth abundant materials. *Sol. Energy Mater. Sol. Cells* **145**, 454–461. https://doi.org/10.1016/j.solmat.2015.11.015 (2016).
65. Moustafa, M., Al Zoubi, T. & Yasin, S. Exploration of CZTS-based solar using the ZrS_2 as a novel buffer layer by SCAPS simulation. *Opt. Mater.* **124**, 112001 (2022).
66. Lin, W. M. M. *et al.* Simulating nanocrystal-based solar cells: A lead sulfide case study. *J. Chem. Phys.* **151**, 241104. https://doi.org/10.1063/1.5129159 (2019).
67. Mbopda Tcheum, G. L., Teyou Ngoupo, A., OuÉDraogo, S., Guirdjebaye, N. & Ndjaka, J. M. B. Numerical analysis of ultrathin $Cu(In, Ga)Se_2$ solar cells with Zn(O, S) buffer layer. *Pramana* **94**, 111. https://doi.org/10.1007/s12043-020-01977-y (2020).
68. Baloch, A. A. B. *et al.* Full space device optimization for solar cells. *Sci. Rep.* **7**, 11984. https://doi.org/10.1038/s41598-017-12158-0 (2017).
69. Al-Hattab, M. *et al.* Numerical simulation of a new heterostructure CIGS/GaSe solar cell system using SCAPS-1D software. *Sol. Energy* **227**, 13–22. https://doi.org/10.1016/j.solener.2021.08.084 (2021).
70. Chen, A. & Zhu, K. Computer simulation of a-Si/c-Si heterojunction solar cell with high conversion efficiency. *Sol. Energy* **86**, 393–397. https://doi.org/10.1016/j.solener.2011.10.015 (2012).
71. Musselman, K. P., Marin, A., Schmidt-Mende, L. & MacManus-Driscoll, J. L. Incompatible length scales in nanostructured Cu_2O solar cells. *Adv. Funct. Mater.* **22**, 2202–2208 (2012).
72. Verschraegen, J. & Burgelman, M. Numerical modeling of intra-band tunneling for heterojunction solar cells in SCAPS. *Thin Solid Films* **515**, 6276–6279 (2007).
73. Zhu, L., Shao, G. & Luo, J. Numerical study of metal oxide hetero-junction solar cells with defects and interface states. *Semicond. Sci. Technol.* **28**, 055004 (2013).
74. Gupta, G. K. & Dixit, A. Theoretical studies of single and tandem Cu_2ZnSn $(S/Se)_4$ junction solar cells for enhanced efficiency. *Opt. Mater.* **82**, 11–20 (2018).
75. Ashraf, M. A. & Alam, I. Numerical simulation of CIGS, CISSe and CZTS-based solar cells with In_2S_3 as buffer layer and Au as back contact using SCAPS 1D. *Eng. Res. Express* **2**, 035015. https://doi.org/10.1088/2631-8695/abade6 (2020).
76. Piñón Reyes, A. C. *et al.* Study of a lead-free perovskite solar cell using CZTS as HTL to achieve a 20% PCE by SCAPS-1D simulation. *Micromachines* **12**, 1508 (2021).
77. Chawki, N., Rouchdi, M. & Fares, B. *Numerical sTudy of $BaZrS_3$ Based Chalcogenide Perovskite Solar Cell Using SCAPS-1D Device Simulation* (2022).
78. Goutham Kumar, S., Pramod, A., Prashanth, C. & Honnavar, G. J. Proposal for a novel perovskite solar cell based on $BaZrS_3$ with optimized electron and hole transport layer using SCAPS-1D. *Eur. Chem. Bull.* **12**, 10289–10307 (2023).
79. Kanoun, M. B., Ul Haq, B., Kanoun, A.-A. & Goumri-Said, S. Ti alloying as a route to $BaZrS_3$ chalcogenide perovskite with enhanced photovoltaic performance. *Energy Fuels* **37**, 9548–9556. https://doi.org/10.1021/acs.energyfuels.3c01272 (2023).
80. Thakur, N., Kumar, P., Neffati, R. & Sharma, P. Design and simulation of chalcogenide perovskite $BaZr(S, Se)_3$ compositions for photovoltaic applications. *Phys. Scr.* **98**, 065921. https://doi.org/10.1088/1402-4896/accfc6 (2023).
81. Barman, B. & Ingole, S. Analysis of Si back-contact for chalcogenide perovskite solar cells based on $BaZrS_3$ using SCAPS-1D. *Adv. Theory Simul.* **6**, 2200820 (2023).
82. VincentMercy, E. N., Srinivasan, D. & Marasamy, L. Emerging BaZrS(3) and Ba(Zr,Ti)S(3) Chalcogenide Perovskite Solar Cells: A Numerical Approach Toward Device Engineering and Unlocking Efficiency. *ACS Omega* **9**, 4359–4376. https://doi.org/10.1021/acsomega.3c06627 (2024).

Acknowledgements

Author contributions

A.A.E.-N.: Data curation, methodology, formal analysis, writing—original draft preparation, writing—reviewing and editing, supervision. L.A.L.: Data curation, methodology, software, writing—original draft preparation, reviewing and editing. A.A.F.: Data curation, methodology, software, writing—original draft preparation, reviewing and editing. W.I.: Data curation, methodology, formal analysis, writing—original draft preparation, writing—reviewing and editing, supervision. M.A.: data curation, methodology, formal analysis, writing- original draft preparation, writing—reviewing and editing, supervision. S.W.S.: Visualization, methodology, investigation, writing—reviewing and editing final version of manuscript. A.E.-S.: Resources, validation, project administration, writing—reviewing and editing, supervision.

Funding

Competing interests

The authors declare no competing interests.

Additional information

Correspondence and requests for materials should be addressed to A.A.E.-N., M.A. or A.E.-S.

Reprints and permissions information is available at www.nature.com/reprints.